

Double isotope-ratio thermometers: The influence of emission time scales

V. E. Viola and K. Kwiatkowski*

Department of Chemistry and Indiana University Cyclotron Facility, Indiana University, Bloomington, Indiana 47405

W. A. Friedman

Department of Physics, University of Wisconsin, Madison, Wisconsin 53715

(Received 25 September 1998)

Isotope ratios are examined for several inclusive studies of light-ion and ^{14}N -induced reactions that involve significantly different reaction dynamics and bombarding energies. For adjacent isotope pairs that have one nuclide with $N < Z$, the ratios show a strong dependence on emission angle. Pairs with only $N \geq Z$ isotopes depend weakly on N/Z of the colliding system, but are otherwise not sensitive to angle of observation or beam energy. The double isotope-ratio method of Albergo has been used to determine apparent nuclear temperatures from these data. When empirically corrected for secondary decay effects, values in the range $T_{\text{iso}} \approx 4.0 \pm 0.4$ MeV are found for forward-angle measurements and $T_{\text{iso}} \approx 2.4 \pm 0.4$ MeV for backward angles. The double isotope-ratio temperatures are found to be systematically lower than temperatures derived from spectral shape analyses and Fermi gas estimates. This difference suggests the importance of time evolution in the application of temperature gauges. Relative emission-time differences between neutron-deficient and heavier isotopes arise from both nonequilibrium emission processes and cooling of the system during statistical decay. The importance of secondary feeding is also pointed out. These effects are illustrated by expanding, emitting source calculations. [S0556-2813(99)05705-2]

PACS number(s): 25.70.Mn, 24.10.Pa, 25.70.Gh

I. INTRODUCTION

Determining the temperature of hot residues formed in energetic nucleus-nucleus collisions is central to experimental efforts to characterize the equation of state in finite nuclei and to identify a possible phase transition in such systems. At low bombarding energies, neutron and charged-particle spectral shapes have historically served this purpose [1,2]. However, in the bombarding-energy regime above $E/A \sim 20$ MeV, the effects of Fermi motion and sequential statistical emission can lead to a broad distribution of emitting sources that introduces major uncertainties in determining temperatures from inclusive spectra [3–6]. Over the past decade, the population-of-excited states method [5,7,8] has been applied successfully to such systems, generally yielding temperatures lower than those indicated by spectral shapes. More recently, Pochodzalla *et al.* [9] have employed a double-isotope-ratio thermometer [10] in analysis of multi-fragmentation data, from which they have proposed a heating curve for the finite nuclear liquid-gas system. Similar analyses have subsequently been performed by several groups [11–14]. The self-consistency of the technique within a given system and comparisons with excited-state populations have been investigated in detail by Tsang and co-workers [15,16].

In this report, the isotope-thermometer technique is applied to inclusive nuclidic-yield data from several studies of light-ion and ^{14}N -induced reactions. The mechanisms for these reactions span a wide range of emission time scales, from prompt nonequilibrium processes to much slower

evaporative phenomena. In order to define the fragment kinetic energy spectra as completely as possible, the measurements reported here have emphasized low energy thresholds for each nuclide in the yield distribution. This is particularly important at backward angles, where the observation of fully equilibrated systems is most probable, but where detector thresholds and kinematics conspire to impose low-energy cutoffs on the spectra.

Following Albergo [10], the isotope yield for a system in chemical and thermal equilibrium can be related to temperature T_{iso} via the expression

$$T_{\text{iso}} = B / \ln(aR), \quad (1)$$

where B is the binding energy difference for the fragments, and a is a factor that accounts for the mass and spin of each fragment. Volume emission at a fixed freeze-out condition having a temperature T_{iso} is assumed in the Albergo analysis. The double isotope ratio R is the ground-state population ratio at freeze-out (Y) for fragments (A, Z) ,

$$R = \frac{Y(A_i, Z_i) / Y(A_i + 1, Z_i)}{Y(A_j, Z_j) / Y(A_j + 1, Z_j)}. \quad (2)$$

Measured yields and related double ratios, however, include the cumulative effects of secondary feeding. In the present analysis, this correction has been made with the empirical systematics of Tsang [15], which define a correction factor $\ln \kappa$ for each double ratio. This procedure relates an apparent temperature T_{app} based on measured yields, R_{exp} , to a freeze-out temperature T_{iso} , where

$$\frac{1}{T_{\text{app}}} = \frac{1}{T_{\text{iso}}} + \frac{\ln \kappa}{B}. \quad (3)$$

*Present address: Los Alamos National Laboratory, Los Alamos, NM 87545.

TABLE I. Ratios of isotope yields, classified in groups of constant isospin.

Ratio	$p + \text{Ag}$	$^4\text{He} + \text{Ag}$	$^4\text{He} + ^{116}\text{Sn}$		$p + \text{Xe}$	$^4\text{He} + ^{124}\text{Sn}$		$^4\text{He} + ^{197}\text{Au}$
E_{proj}	480 MeV	200 MeV	200 MeV	180 MeV	300 GeV	200 MeV	180 MeV	200 MeV
θ_{obs}	160°	20°	12°	154°		12°	154°	20°
$(N/Z)_{\text{CN}}$	1.27	1.29	1.31	1.31	1.44	1.46	1.46	1.48
$^{11}\text{C}/^{12}\text{C}$	0.12	0.20	0.40	0.069	0.22	0.20	0.045	0.22
$^{13}\text{N}/^{14}\text{N}$		0.12			0.12			0.082
$^{15}\text{O}/^{16}\text{O}$	0.063	0.18			0.12			0.11
$^{17}\text{F}/^{18}\text{F}$	0.14				0.19			
$^6\text{Li}/^7\text{Li}$	0.86	0.75	0.92	0.86	0.40	0.70	0.43	0.52
$^{10}\text{B}/^{11}\text{B}$	0.54	0.64	0.63	0.40	0.32	0.52	0.22	0.44
$^{12}\text{C}/^{13}\text{C}$	1.5	1.6	1.9	1.6	0.91	1.8	0.91	1.0
$^{14}\text{N}/^{15}\text{N}$	0.49	0.59			0.34			0.44
$^{16}\text{O}/^{17}\text{O}$	1.8	1.9			1.4			1.4
$^{18}\text{F}/^{19}\text{F}$	0.42				0.37			
$^{20}\text{Ne}/^{21}\text{Ne}$	0.74				0.48			
$^7\text{Li}/^8\text{Li}$		7.4	7.6	9.0	3.4	6.0	5.9	5.2
$^9\text{Be}/^{10}\text{Be}$	3.2	1.9	1.8	2.5	1.0	1.3	1.4	1.3
$^{11}\text{B}/^{12}\text{B}$	6.3	8.2	8.4	6.6	3.9	7.5	3.8	4.8
$^{13}\text{C}/^{14}\text{C}$	2.6	3.0	3.9	2.6	1.8	3.6	1.5	1.9
$^{15}\text{N}/^{16}\text{N}$	6.4	7.3			4.5			4.4
$^{17}\text{O}/^{18}\text{O}$	1.5	1.5			1.0			0.82
$^{19}\text{F}/^{20}\text{F}$	1.2				1.0			
$^{21}\text{Ne}/^{22}\text{Ne}$	0.82				0.87			
$^8\text{Li}/^9\text{Li}$	7.1	6.1	5.9	11.5	3.4	4.8	5.1	3.2
$^{12}\text{B}/^{13}\text{B}$	6.1	4.9	5.5	4.9	2.7	4.0	2.9	3.3
$^{14}\text{C}/^{15}\text{C}$		8.4		8.8	6.5		4.5	6.8
$^{16}\text{N}/^{17}\text{N}$	2.2	2.1			3.3			2.8
$^{18}\text{O}/^{19}\text{O}$	7.3	4.6			1.7			1.4
$^{20}\text{F}/^{21}\text{F}$	1.5				1.8			
$^{22}\text{Ne}/^{23}\text{Ne}$	3.7			3.1				
Ref.	[17]	[18]	[19]	[19]	[20]	[19]	[19]	[18]

In determining the value of T_{app} for all possible combinations of isotopes for each system, only those ratios for which $B \geq 10$ MeV were included, since studies by Tsang *et al.* [15] have shown the smallest fluctuations for such combinations. In order to satisfy this binding energy requirement, one, and only one, nuclide with neutron number $N < Z$ must be included in the double-isotope ratio.

In the present study we first examine double-isotope-ratio temperatures determined from isotopically resolved intermediate-mass fragment (IMF: $Z = 3 - 12$) spectra produced in light-ion-induced reactions [17–20]. All double ratios involve either the $^{11}\text{C}/^{12}\text{C}$ or $^{15}\text{O}/^{16}\text{O}$ pairs. For the data from Refs. [17] and [19], measurements are available at both forward angles, where nonequilibrium processes dominate the spectra for fragments up to $Z \sim 6$, and backward angles, where emission has been shown to be consistent with emission from an equilibrated composite system with $> 90\%$ of the beam momentum [21]. Next, this technique is employed to determine T_{iso} values from $^2\text{H}/^3\text{H}$ and $^3\text{He}/^4\text{He}$ spectra in several other light-ion systems [14,22–24]. And finally, data are analyzed for $Z = 3 - 8$ isotopes formed in the $^{14}\text{N} + ^{\text{nat}}\text{Ag}$, ^{197}Au reactions [4] at bombarding energies between $E/A = 20 - 100$ MeV, again using either the $^{11}\text{C}/^{12}\text{C}$ or

$^{15}\text{O}/^{16}\text{O}$ ratio as one of the pairs. The isotope ratio measurements in the ^{14}N studies were performed at angles where equilibrium and nonequilibrium emission are of comparable importance [4]. The temperature evolution of highly excited nuclear matter and secondary feeding effects during fragment cooling are also examined in the context of the statistical expanding, evaporating source (EES) model [25].

The 300-GeV $p + ^{\text{nat}}\text{Xe}$ results [20] are included as a reference point. These data provide an extensive set of isotope ratios measured with low thresholds, and have previously been subjected to a double-isotope-ratio analysis [15]. Thus, the data sets examined here permit a broad sampling of the sensitivity of T_{iso} to bombarding energy, target-projectile N/Z and reaction mechanism.

II. IMF ISOTOPE-RATIO TEMPERATURES FROM LIGHT-ION-INDUCED REACTIONS

In Table I, single ratios of adjacent isotopes $Y(A, Z)/Y(A + 1, Z)$ from Refs. [17–20] are tabulated for pairs of IMFs, grouped according to constant neutron-proton difference $N - Z$ of the lighter isotope of the pair. Also listed are the angle of observation and the N/Z ratio of the collid-

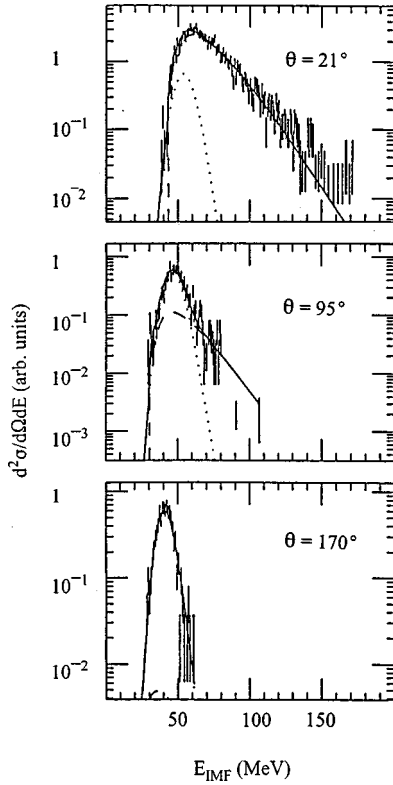


FIG. 1. Spectrum of carbon fragments emitted at forward, intermediate, and backward angles from the 200-MeV ${}^4\text{He}+{}^{197}\text{Au}$ reaction [18]. Two-component moving-source fits to the data are described by dotted line (equilibrium component), dashed line (nonequilibrium component), and solid line (sum). At 21° the nonequilibrium and sum curves overlap; at 170° the equilibrium and sum curves overlap.

ing system. Ratios involving H and He isotopes are discussed in Sec. III.

First, we consider those single ratios that contain one neutron-deficient ($N=Z-1$) isotope. One of these must be included in Eq. (1) in order for the binding-energy parameter B to exceed 10 MeV. For ratios involving a neutron-deficient nuclide (e.g., ${}^{11}\text{C}/{}^{12}\text{C}$), the forward-angle values are systematically a factor of about five higher than those at backward angles. The mechanisms responsible for the angular dependence of the single ratios are suggested by the kinetic-energy spectra in Fig. 1 [18]. Here inclusive isotope-integrated spectra for carbon fragments emitted at representative forward, intermediate and backward angles are shown for the 200-MeV ${}^4\text{He}+{}^{197}\text{Au}$ reaction. These data have been analyzed with a moving-source model that assumes two components: one corresponding to fast nonequilibrium emission and a second described by the decay of an equilibrated residue. As shown by the source decomposition in Fig. 1, the fast source dominates the forward-angle yield, whereas the equilibrated source accounts for most of the yield in the backward hemisphere. This suggests that the larger single ratios at forward angles are most likely attributable to nonequilibrium processes. Consistent with this argument, studies of isotopically-resolved spectra at forward angles [4,17–19,26,27] show that neutron-deficient isotopes have distinctly flatter spectral shapes (i.e., higher spectral temperatures) than those with $N \geq Z$.

TABLE II. Average of each single isotope ratio relative to the corresponding value for the $p+\text{Xe}$ system in Table I, where $\langle R_{\text{single}} \rangle = \langle [Y_i(A,Z)/Y_i(A+1,Z)]/[Y_{\text{Xe}}(A,Z)/Y_{\text{Xe}}(A+1,Z)] \rangle$. The second column lists the N/Z ratio of the target-projectile system and the third column gives the angle of observation. Also given are representative ratios for ${}^{14}\text{N}+{}^{\text{nat}}\text{Ag}$, ${}^{197}\text{Au}$ reactions. Isotopes with $N < Z$ are not included.

System	$(N/Z)_{\text{CN}}$	θ_{obs}	$\langle R_{\text{single}} \rangle$
700 MeV ${}^{14}\text{N} + \text{Ag}$	1.26	40°	0.64 ± 0.07
1140 MeV ${}^{14}\text{N} + \text{Ag}$	1.26	20°	0.63 ± 0.08
480 MeV $p + \text{Ag}$	1.27	20°	0.73 ± 0.12
480 MeV $p + \text{Ag}$	1.27	160°	0.78 ± 0.14
200 MeV ${}^4\text{He} + \text{Ag}$	1.29	20°	0.61 ± 0.18
200 MeV ${}^4\text{He} + {}^{116}\text{Sn}$	1.31	12°	0.57 ± 0.14
180 MeV ${}^4\text{He} + {}^{116}\text{Sn}$	1.31	154°	0.60 ± 0.19
3 GeV $p + \text{Xe}$	1.41	48°	1.00
1400 MeV ${}^{14}\text{N} + {}^{197}\text{Au}$	1.45	20°	1.03 ± 0.18
200 MeV ${}^4\text{He} + {}^{124}\text{Sn}$	1.46	12°	0.75 ± 0.20
180 MeV ${}^4\text{He} + {}^{124}\text{Sn}$	1.46	154°	1.00 ± 0.21
200 MeV ${}^4\text{He} + {}^{197}\text{Au}$	1.48	20°	0.96 ± 0.21

Next, we consider the ratios for the 22 pairs of adjacent isotopes with $N \geq Z$. These isotopes comprise about 95% of the absolute IMF yield for the systems in Table I. In contrast to the case for ratios involving an $N < Z$ isotope, these single ratios are approximately independent of emission angle, bombarding energy or target-projectile system. The variation for a given single ratio (e.g., ${}^{12}\text{C}/{}^{13}\text{C}$) among all systems is less than a factor of three, part of which can be accounted for by a systematic increase in the yields of neutron-excess isotopes as the N/Z ratio of the composite system increases [19,28]. The N/Z dependence tends to cancel out in the double-isotope procedure [29]. The lack of dependence on reaction mechanism for the single ratios involving only $N \geq Z$ isotopes is not fully understood, but may be related to the independence of isotope ratios on excitation energy, as suggested by the EES calculations discussed below.

To illustrate the uniformity of the yields quantitatively, all $(Z,A)/(Z,A+1)$ ratios involving only $N \geq Z$ isotopes have been normalized to the corresponding ratios for 300 GeV $p + {}^{\text{nat}}\text{Xe}$ data [20]. These ratios are near unity in all cases. The normalized ratios, averaged over all isotope pairs are shown in Table II. Based on this comparison and the relatively small standard deviations, it would appear possible to estimate the isotope ratio for a given pair with $N \geq Z$ at all angles for light-ion-induced reactions by scaling to the $p + \text{Xe}$ results and taking into account the N/Z of the composite system. The implication of this isotope-ratio constancy is that the $N \geq Z$ pairs in Eq. (2) provide little sensitivity for determining T_{iso} due to the logarithmic dependence on R .

From the data listed in Table I, values of T_{app} have been calculated for all pairs with $B > 10$ MeV, using Eqs. (1) and (2). All the ratios R contain ${}^{11}\text{C}/{}^{12}\text{C}$ or ${}^{15}\text{O}/{}^{16}\text{O}$ in the denominator of Eq. (2). Corrections for secondary feeding using Eq. (3) and the values of $\ln \kappa/B$ from Ref. [15] have been applied to derive values of T_{iso} for each ratio. These have then been averaged to yield average values of $\langle T_{\text{iso}} \rangle$, listed in Table III. These values are not yield-weighted.

At forward angles, all values fall in the range $\langle T_{\text{iso}} \rangle$

TABLE III. Temperature comparisons for light-ion-induced reactions derived from $^{11}\text{C}/^{12}\text{C}$ and $^{15}\text{O}/^{16}\text{O}$ ratios.

System	θ_{obs}	$\langle T_{\text{iso}} \rangle$ (MeV)	$T_{\text{FG}}^{\text{MAX}}$ (MeV)	$\langle T_{\text{EQ}}^{\text{MS}} \rangle$ (MeV)	Ref.
480-MeV $p + ^{\text{nat}}\text{Ag}$	20°	4.3 ± 0.9			
	160°	2.8 ± 0.2			
200-MeV $^4\text{He} + ^{\text{nat}}\text{Ag}$	20°	3.5 ± 0.2	3.7	3.7	[17]
200-MeV $^4\text{He} + ^{116}\text{Sn}$	12°	3.6 ± 0.2	3.4		
180-MeV $^4\text{He} + ^{116}\text{Sn}$	154°	2.6 ± 0.3	3.4	3.4 ± 0.2	[18]
300-GeV $p + \text{Xe}$		3.9 ± 0.2	NA		[19]
200-MeV $^4\text{He} + ^{124}\text{Sn}$	12°	4.3 ± 0.3	3.3		
180-MeV $^4\text{He} + ^{124}\text{Sn}$	154°	2.7 ± 0.3	3.3	3.4 ± 0.2	[18]
200-MeV $^4\text{He} + ^{197}\text{Au}$	20°	3.7 ± 0.2	2.8	2.8	[17]

θ_{obs} : laboratory angle of observation

$T_{\text{FG}}^{\text{MAX}}$: calculated assuming $a = A/8 \text{ MeV}^{-1}$

$\langle T_{\text{EQ}}^{\text{MS}} \rangle$: temperature from moving-source fits to equilibrium (EQ) component of the spectrum; averaged over $Z = 5 - 10$ IMFs.

$\langle T_{\text{iso}} \rangle$: temperature from double-isotope ratios; averaged over all pairs with $B \geq 10$ MeV.

$\cong 3.6 - 4.3$ MeV, comparable to the 300-GeV $p + ^{\text{nat}}\text{Xe}$ data [15,20]. There is little correlation with bombarding energy or composite system. A similar system to those in Table I, 200-MeV $^3\text{He} + ^{\text{nat}}\text{Ag}$, has been studied to determine temperatures via the population-of-excited-states method [30]. At forward angles a value of 4 MeV is obtained, nearly the same as for $\langle T_{\text{iso}} \rangle$ values from the double-isotope thermometer. This correspondence between the isotope-ratio temperatures and those from the population-of-excited states method has also been noted in $E/A = 50 - 200$ MeV $^{197}\text{Au} + ^{197}\text{Au}$ collisions by Serfling *et al.* [31], where similar temperature values were obtained. However, while there is general consistency between the two thermometers, it must be kept in mind that in our case they are being applied to reactions believed to occur on a very fast time scale, and hence the assumption of equilibrium distributions may not be applicable for either the excited state population or the isotope ratios. The backward-angle data yield lower values, $\langle T_{\text{iso}} \rangle \cong 2.0 - 2.8$ MeV. This is somewhat higher than the value of ~ 1 MeV obtained from the backward-angle measurements via the population-of-excited-states method in Ref. [30].

Thus, both the isotope-ratio temperatures and those from excited-state populations seem consistent with a picture in which fragments emitted at forward angles contain a significant contribution from processes that occur on a short time scale from a hot, localized region of the nucleus [32]. At backward angles the ejectiles appear to be produced in cooler, thermalized events. However, even for nearly equilibrated systems, there may not be a simple freeze-out condition. The emission of $N < Z$ isotopes may occur at earlier times (i.e., higher average excitation energies) than for those with $N \geq Z$, as suggested by the EES model [25]. This is a consequence of the slightly higher Coulomb barriers and the large cost in binding energy required to produce neutron-deficient fragments, discussed in more detail in the following section.

Insight into the relative constancy of the $\langle T_{\text{iso}} \rangle$ values for widely different systems may be gained from EES calculations. The effect of initial excitation energy on the isotope ratios predicted by the EES model is shown in Fig. 2 for a

^{107}Ag nucleus. All values are relative. The top panel of Fig. 2 shows EES calculations of two carbon isotope ratios, $^{11}\text{C}/^{12}\text{C}$ and $^{12}\text{C}/^{13}\text{C}$ from a range of excitation energies in a decaying ^{107}Ag system. A strong dependence on E^* is observed for the former, whereas the latter ratio shows only a weak dependence. Similar behavior for $^3\text{He}/^4\text{He}$ and $^3\text{H}/^2\text{H}$ ratios in the lower panel of Fig. 2, is discussed in the next section.

It is also important to consider the cooling of the hot fragments themselves. Feeding effects at the end of the de-excitation chain can significantly alter the primary isotope ratios, as shown in Fig. 3 for an EES calculation of the $p + ^{131}\text{Xe}$ system heated to an initial temperature of $T = 10$ MeV. The calculated ratios are all normalized to the $p + \text{Xe}$ yield data of Ref. [20]. Single isotope ratios for three calculational cases are shown: primary distribution only (no feeding), gamma-ray feeding only, and both gamma-ray and particle feeding. The strong perturbations of the ratios due to feeding are apparent. This serves to emphasize the important distinction between T_{app} and T_{iso} . One notes in Fig. 3 that those isotopes least affected by feeding are the neutron-excess isotopes of the odd- Z IMFs Li and B.

III. LCP ISOTOPE-RATIO TEMPERATURES

The effects of emission time scale become increasingly important for T_{app} values derived from LCP ratios (LCP = H and He isotopes). Two primary concerns involving these isotopes are (1) the known increase in $^3\text{He}/^4\text{He}$ ratios with increasing fragment kinetic energy due to nonequilibrium/cooling effects [14,17,27,33], and (2) secondary decay of heavier fragments to produce light-charged particles especially ^4He . In Table IV we examine several studies where equilibrated charged-particle emission [22–24] has been reported. Here only the $^{2,3}\text{H}/^{3,4}\text{He}$ thermometer can be used due to low yields for heavier fragments.

The 55-MeV $^3\text{He} + ^{\text{nat}}\text{Ag}$ spectra [24], have recently been measured at backward angles to high precision (Fig. 4). These spectra should be representative of an equilibrated system formed with (nearly) complete momentum transfer.

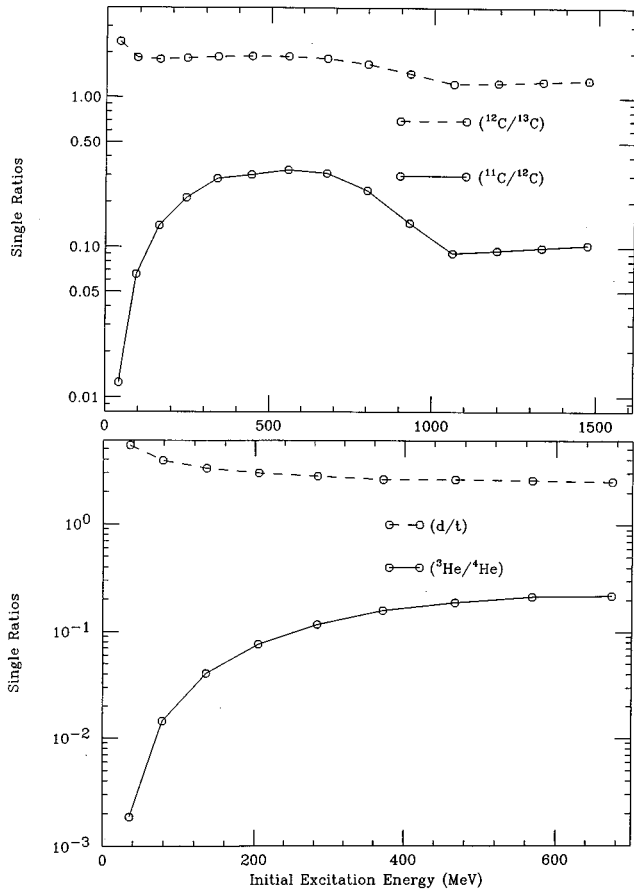


FIG. 2. Single isotope ratios predicted by EES model as a function of initial excitation energy for an Ag nucleus. Top panel: solid curve is for $^{11}\text{C}/^{12}\text{C}$ ratio; dashed curve is for $^{12}\text{C}/^{13}\text{C}$. Bottom panel: solid curve is for $^3\text{He}/^4\text{He}$ ratio; dashed curve is for $^2\text{H}/^3\text{H}$ ratio. Note differences in both ordinate and abscissa scales for carbon fragments relative to plot for He isotopes.

From the spectral shapes it is apparent that the $^3\text{He}/^4\text{He}$ ratio changes dramatically with emitted fragment kinetic energy. Integration of the full yield, however, leads to isotope-ratio temperatures generally consistent with the Fermi gas estimates or spectral-shape analyses. For the 55-MeV case one obtains $T_{\text{iso}}=2.0$ MeV and $^3\text{He}/^4\text{He}=0.0055$, compared with $T_{\text{FG}}=2.2$ MeV $a \approx A/8$ MeV $^{-1}$). EES calculations yield $T_{\text{app}}=1.9$ MeV with $^3\text{He}/^4\text{He}=0.004$, reflecting some neutron cooling. The results in Table IV for the 95-MeV case suggest a lower average linear momentum transfer [21,34].

The 140-MeV ^4He -induced reaction, for which the data were decomposed into equilibrium and nonequilibrium components [22], yield results generally consistent with Table III in that both analyses yield much higher isotope-ratio temperatures for the nonequilibrium component, $T_{\text{iso}} \approx 5-6$ MeV. For the lower-energy-proton inclusive data [23], T_{app} values higher than the Fermi gas expectation are obtained. This may be explained by the inclusion of a significant pre-equilibrium component in the ratios, which can strongly affect T_{app} . In addition, it should be stressed that the Alberg model assumes many cancellations that may be valid at high excitation energies, but not for reactions much nearer the barrier. Thus, some of the data in Table IV may invoke the model in a regime where its applicability is limited.

At much higher bombarding energies, the effects of emission time scale on $^3\text{He}/^4\text{He}$ ratios become more dramatic. This is illustrated in Fig. 5 where the $^3\text{He}/^4\text{He}$ ratio obtained with a minimum-bias trigger is plotted as a function of kinetic energy for a multifragmenting system, 4.8-GeV $^3\text{He} + \text{nat Ag}, ^{197}\text{Au}$ [14,35]. The $^3\text{He}/^4\text{He}$ ratio has been used in most caloric curve analyses to date [9,11-14]. For the most energetic He isotopes, nonequilibrium effects may dominate the ratios. Another interpretation of the observed increase in the $^3\text{He}/^4\text{He}$ ratio with He energy is that it provides an ‘‘instantaneous temperature’’ of the source as it evolves toward equilibrium, in the spirit of the accreting source model of Fields *et al.* [32]. The large increase in the $^3\text{He}/^4\text{He}$ ratio as a function of He energy also points to the possible uncertainties associated with detector identification thresholds and energy-acceptance windows in determining cumulative yields. Thus, careful selection criteria must be imposed in determining the appropriate $^3\text{He}/^4\text{He}$ ratio for the breakup stage.

Differences in emission times for equilibrated systems are predicted by the EES model [25]. In the EES model, surface emission of IMFs occurs from an expanding, cooling source. At sufficiently high temperatures, cluster formation in the dilute system leads to disassembly, at which point volume emission is assumed. Corresponding EES predictions are shown in Fig. 6 for the temperature(time) evolution of He isotopes emitted from a ^{197}Au nucleus initially heated to $T=15$ MeV, which should be representative of this system.

Due to expansion, breakup for this system occurs at a temperature of $T \sim 5-6$ MeV; secondary decay effects are included in the calculations. The preferential emission of ^3He early in the cooling process is apparent in Fig. 6. Nearly 50% of the ^3He yield is emitted by the time the temperature has cooled to $T \approx 10$ MeV; i.e., after ~ 25 fm/c. For ^4He this fraction is not reached until the system has reached the breakup/volume-emission regime near $T \sim 6$ MeV, or ~ 70 fm/c. Overall the average emission temperature is $\langle T \rangle = 9.9$ MeV for ^3He and 6.7 MeV for ^4He . Thus, the He isotope ratios are strongly time-dependent, even in the context of an equilibrium model.

For IMFs, this picture changes significantly, as shown in Fig. 7. Here calculations employing the EES model [25] have been used to predict the evolution of $^{11,13}\text{C}$ isotope yields as a function of thermodynamic temperature, also for a ^{197}Au nucleus heated to an initial temperature of $T=15$ MeV. Although IMF emission is shown to be primarily associated with the low-density breakup phase of the reaction at these excitation energies, it is observed that the $N < Z$ isotope is produced at all temperatures, whereas nearly the entire $N > Z$ yield comes from the final breakup of the system. The yield-weighted average temperature difference is small, however, $\langle T \rangle = 5.8$ MeV for ^{11}C and $\langle T \rangle = 5.4$ MeV for ^{13}C . These calculations indicate that for heavy fragments such as carbon, the statistical-emission time does not cause a strong perturbation of the isotope-ratio temperatures. However, the results indicate that heavy fragments sample the temperature very late in the cooling process. The upshot of Figs. 6 and 7 is that He isotope ratios may be much affected by the entire sequence of events during the cooling of very hot nuclei, whereas ratios for heavier IMFs appear to be better probes of the conditions during the breakup stage of

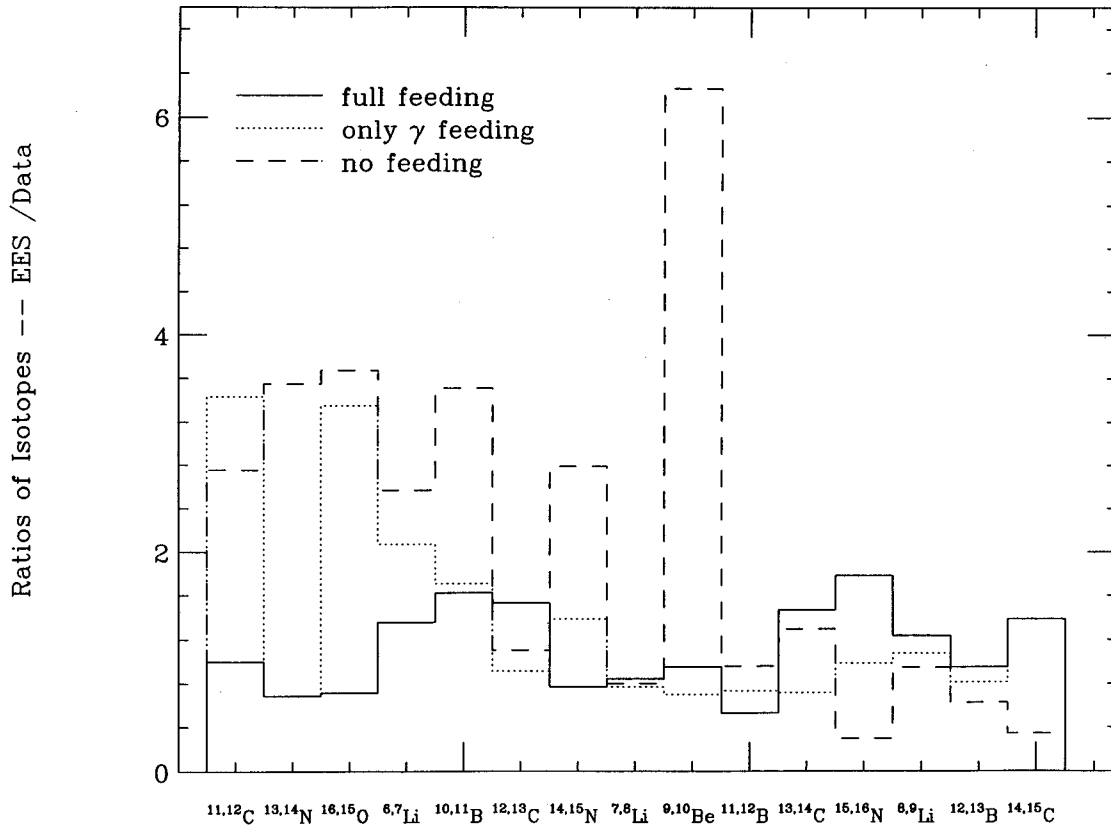


FIG. 3. Ratios of EES model predictions to data from 300 GeV $p + \text{Xe}$ measurements [20] for a Xe nucleus heated to a temperature of 10 MeV. Dashed line is for case of no feeding, dotted line includes feeding due to gamma rays, and solid line is for both gamma-ray and charged-particle feeding.

multifragmentation. In either case, however, in the context of the EES scenario, the isotope-ratio temperature should be regarded as a time-averaged temperature and not a unique thermodynamic temperature at a single freeze-out condition.

IV. IMF ISOTOPE-RATIO TEMPERATURES IN ^{14}N -INDUCED REACTIONS

In Fig. 8 and Table V we examine the bombarding energy dependence of the isotope thermometer method for IMFs

produced in the $^{14}\text{N} + \text{natAg}$, ^{197}Au reactions between $E/A = 20\text{--}100$ MeV [4,34]. Isotope measurements were performed at angles between $20^\circ\text{--}50^\circ$. In order to emphasize equilibrium-like events, only the lowest part of each fragment spectrum, $(E/A)_{\text{IMF}} \leq 10$ MeV was used to determine the ratios. However, the values of T_{iso} are relatively independent of fragment energy, although the lowest energy fragments systematically yield the lowest isotope-ratio temperatures, as shown in Fig. 9. Little dependence of T_{iso} on angle is observed over this limited angular range. The isotope ra-

TABLE IV. Isotope ratios for $^3\text{He}/^4\text{He}$ for several light-ion-induced reactions and T_{iso} values derived from this ratio. Also listed are Fermi gas temperatures assuming complete fusion and $a = A/8 \text{ MeV}^{-1}$.

System	Source	$^3\text{He}/^4\text{He}$	T_{HHe} (MeV)	$T_{\text{FG}}^{\text{MAX}}$ (MeV)	Ref.
55-MeV $^3\text{He} + \text{natAg}$	147.5°	0.0055	2.0	2.2	[24]
95-MeV $^3\text{He} + \text{natAg}$	147.5°	0.0071	2.1	2.8	[24]
140-MeV $^4\text{He} + ^{90}\text{Zr}$	EQ ^b	0.017	2.3	3.5	[22]
	NEQ ^b	0.25	5.8		[22]
140-MeV $^4\text{He} + ^{209}\text{Bi}$	EQ ^b	0.031	3.0	2.3	[22]
	NEQ ^b	0.17	5.2		[22]
40-MeV $p + ^{209}\text{Bi}$	^a	0.05	3.0	1.2	[23]
62-MeV $p + ^{120}\text{Sn}$	^a	0.04	3.2	2.0	[23]
62-MeV $p + ^{197}\text{Au}$	^a	0.06	3.1	1.6	[23]
62-MeV $p + ^{209}\text{Bi}$	^a	0.06	3.3	1.5	[23]

^aAngle-integrated yields.

^bSource decomposition of angle-integrated yields.

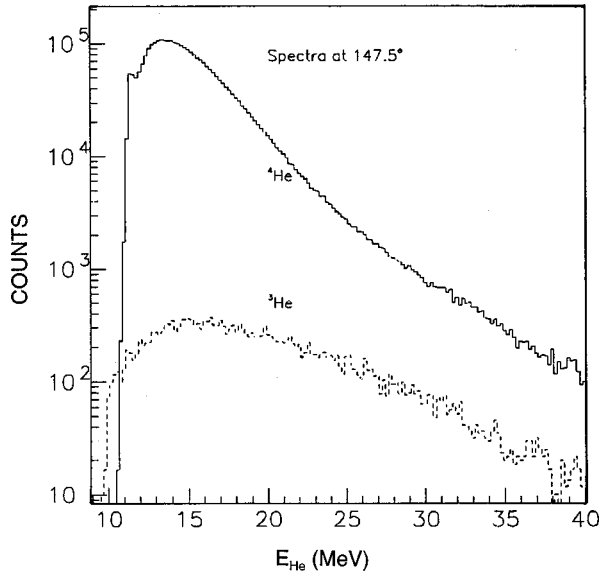


FIG. 4. Spectra of ${}^3\text{He}$ and ${}^4\text{He}$ ions from 55-MeV ${}^3\text{He}$ + ${}^{\text{nat}}\text{Ag}$ reaction at 147.5° [24].

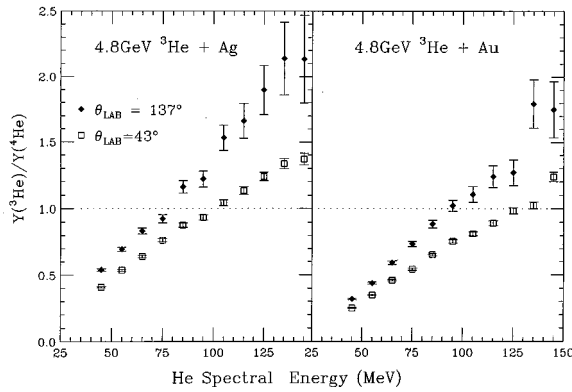


FIG. 5. Ratio of ${}^3\text{He}/{}^4\text{He}$ as a function of He kinetic energy for 4.8 GeV ${}^{\text{nat}}\text{Ag}$, ${}^{197}\text{Au}$ reactions.

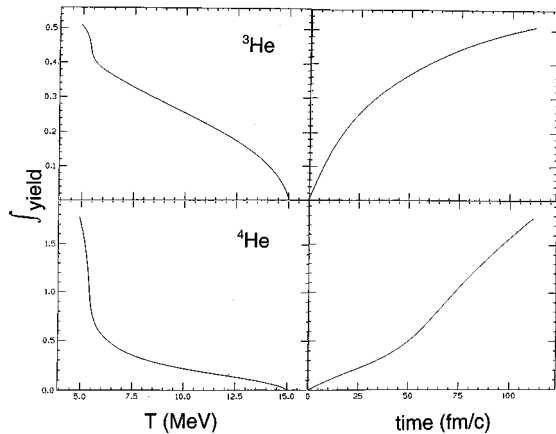


FIG. 6. EES predictions of integrated yield for ${}^3\text{He}$ (upper) and ${}^4\text{He}$ (lower) fragments as function of temperature (left) and time (right) for a ${}^{197}\text{Au}$ nucleus heated to $T=15$ MeV. For this system, the transition from the evaporative to the breakup/volume-emission regime occurs near $T \approx 6$ MeV.

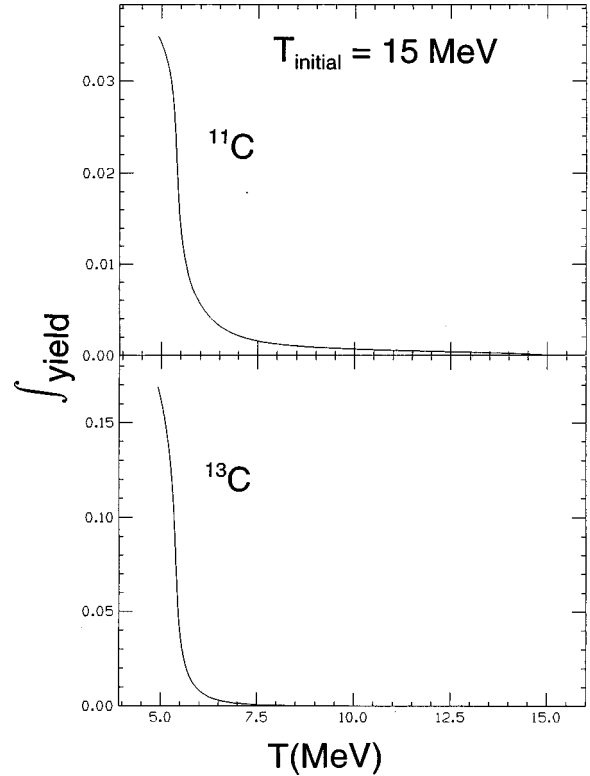


FIG. 7. EES predictions of integrated yield for ${}^{11}\text{C}$ (upper) and ${}^{13}\text{C}$ (lower) fragments as a function of temperature for a ${}^{197}\text{Au}$ nucleus heated to $T=15$ MeV. For this system, the transition from the evaporative to the breakup/volume-emission regime occurs near $T \sim 6$ MeV.

tios for these systems strongly resemble those in Table I for corresponding target and observation angles. In addition, these same experiments measured complete energy spectra for Z-identified fragments over the full angular range. This

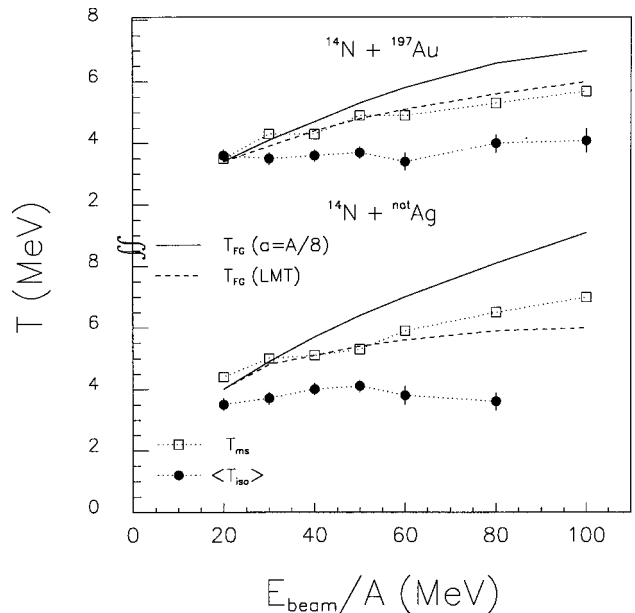


FIG. 8. Bombarding-energy dependence for average isotope-temperature $\langle T_{\text{iso}} \rangle$, moving-source slope temperature $T_{\text{MS}}^{\text{EQ}}$ for equilibrium-like IMFs, and Fermi-gas temperature T_{FG} for $E/A = 20$ – 100 MeV ${}^{14}\text{N} + {}^{\text{nat}}\text{Ag}$, ${}^{197}\text{Au}$ reactions.

TABLE V. Values of $\langle T_{\text{iso}} \rangle$ for several ^{14}N -induced reactions on Ag and Au. Headings are the same as in Table III.

System	N/Z_{CN}	θ_{obs} (deg)	$\langle T_{\text{iso}} \rangle$ (MeV)	$T_{\text{FG}}^{\text{MAX}}$ (MeV)	$\langle T_{\text{EQ}}^{\text{MS}} \rangle$ (MeV)
280-MeV $^{14}\text{N} + \text{natAg}$	1.26	20–40	3.5 ± 0.2	4.0	4.4
420-MeV $^{14}\text{N} + \text{natAg}$		20–40	3.7 ± 0.2	4.9	5.0
560-MeV $^{14}\text{N} + \text{natAg}$		20–40	4.0 ± 0.2	5.7	5.1
700-MeV $^{14}\text{N} + \text{natAg}$		20–40	4.1 ± 0.2	6.4	5.3
840-MeV $^{14}\text{N} + \text{natAg}$		50	3.8 ± 0.3	7.0	5.9
1120-MeV $^{14}\text{N} + \text{natAg}$		20	3.6 ± 0.3	8.1	6.5
280-MeV $^{14}\text{N} + ^{197}\text{Au}$	1.45	30	3.6 ± 0.2	3.5	3.5
420-MeV $^{14}\text{N} + ^{197}\text{Au}$		30	3.5 ± 0.2	4.1	4.3
560-MeV $^{14}\text{N} + ^{197}\text{Au}$		30	3.6 ± 0.2	4.7	4.3
700-MeV $^{14}\text{N} + ^{197}\text{Au}$		30	3.7 ± 0.2	5.3	4.9
840-MeV $^{14}\text{N} + ^{197}\text{Au}$		50	3.4 ± 0.3	5.7	4.9
1120-MeV $^{14}\text{N} + ^{197}\text{Au}$		50	4.0 ± 0.3	6.6	5.3
1400-MeV $^{14}\text{N} + ^{197}\text{Au}$		50	4.1 ± 0.3	7.0	5.7

permitted high quality two-component, moving-source fits to the data, from which spectral slope temperatures could be determined for the equilibrium-like source $T_{\text{MS}}^{\text{EQ}}$ and nonequilibrium source $T_{\text{MS}}^{\text{NEQ}}$ [4,34]. The moving-source temperatures were strongly constrained by the backward-angle spectra, which exhibited the isotropy expected of a thermalized source.

Average temperatures $\langle T_{\text{iso}} \rangle_{\text{EQ}}$ are plotted along with $T_{\text{MS}}^{\text{EQ}}$ values in Fig. 8 as a function of bombarding energy/nucleon for these systems. In calculating $\langle T_{\text{iso}} \rangle$, only $^{11}\text{C}/^{12}\text{C}$ and $^{15}\text{O}/^{16}\text{O}$ ratios were employed for the pair with $N < Z$. The ^{13}N yield was too low to obtain results. The average isotope-ratio temperatures for all systems fall in the range $T_{\text{iso}} = 3.4\text{--}4.1$ MeV. These values are similar to those for non-equilibrium emission observed with light ions in Sec. II. Also shown in Fig. 8 are predictions of a simple Fermi-gas model T_{FG} with level-density parameter $a = A/8$ MeV $^{-1}$.

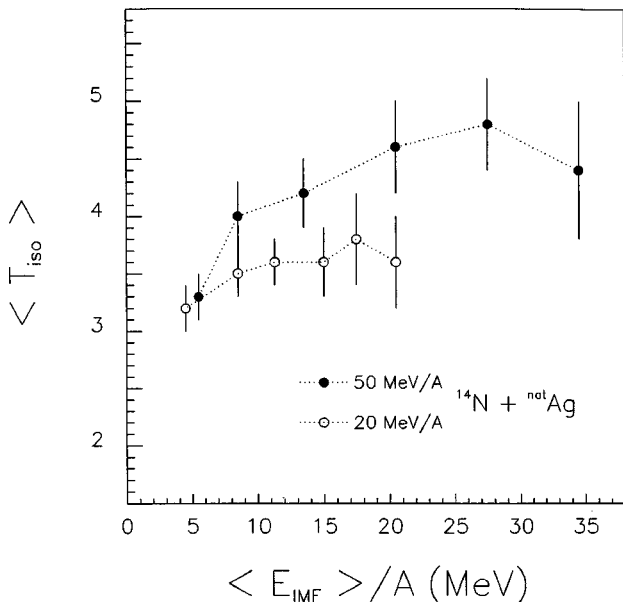


FIG. 9. Plot of $\langle T_{\text{iso}} \rangle$ as a function of $(E/A)_{\text{IMF}}$ measured in the angular range $20^\circ\text{--}40^\circ$ for 280-MeV and 700-MeV $^{14}\text{N} + \text{natAg}$ reactions.

Two assumptions about the reaction dynamics are made in calculating the excitation energy: one assuming complete fusion and a second that includes corrections for incomplete linear momentum transfer [36]. The Fermi-gas predictions that account for incomplete linear momentum transfer are in relatively good agreement with the spectral slope temperatures, but well above the isotope-ratio temperatures at the higher bombarding energies. The difference between the slope and isotope-ratio temperatures suggests that the former values reflect the earlier stages of the cooling process, whereas the latter are more representative of later stages in the cooling of the fragments themselves.

Similar differences between isotope-ratio and slope temperatures are also observed in the data for the $^4\text{He} + \text{Sn}$ reactions, summarized in Table III. Most relevant is the T_{iso} vs $T_{\text{MS}}^{\text{EQ}}$ temperature comparison at backward angles—where equilibrated emission should dominate the complex fragment yield. Here we assume full-momentum-transfer collisions and a level density parameter $a = A/8$ MeV $^{-1}$ in the calculation of T_{FG} . The assumption that complex fragments emitted at backward angles originate from an equilibrated complete-fusion residue is based on the observation of isotropic angular distributions in the backward hemisphere [3,4,18], the sharply-rising nature of the complex fragment excitation functions in this projectile E/A range [37], and IMF-fission-fission correlation studies on heavier targets [21,34]. Possible contributions from incomplete momentum transfer processes will lower the T_{FG} values systematically; this precludes the listing of similar values for the proton-induced reactions. The results show significantly lower values for the isotope-ratio thermometer compared to the moving-source fit temperatures and the Fermi-gas predictions. Thus, these light-ion systems, where equilibrated emission can be isolated, yield the same conclusions as those for ^{14}N .

V. CONCLUSIONS

In summary, isotope-ratios have been examined for several light-ion and ^{14}N -induced reactions where both nonequilibrium and equilibrium fragment emission can be isolated.

Ratios for a given pair of adjacent isotopes, both with $N \geq Z$, show a uniform behavior for all systems, with a weak dependence on target-projectile N/Z . Higher N/Z composite systems produce a higher yield of neutron-excess isotopes. When empirically corrected for secondary decay effects, double isotope-ratio temperatures for inclusive light-ion-induced reactions below about 1 GeV show consistent values of $T_{\text{iso}} \approx 4$ MeV for forward-angle-emission (nonequilibrium), *independent* of bombarding energy, colliding system or reaction dynamics. At extreme backward angles, where equilibrated emission dominates, lower temperatures are obtained, $T_{\text{iso}} \approx 2.5$ MeV. Thus, the results are consistent with a picture in which nonequilibrium emission occurs from a hot localized system, whereas equilibrium emission originates in cooler, fully thermalized sources.

We point out that nonequilibrium processes favor $N < Z$ products, an effect that contributes to strong variations in ${}^3\text{He}/{}^4\text{He}$ ratios with He energy. This dependence on fragment kinetic energy can produce significant variations in calculated isotope-ratio temperatures, depending on experimental thresholds and energy acceptance windows. We also find the isotope-thermometer temperatures to be nearly independent of bombarding energy over a 1 GeV bombarding energy range for ${}^{14}\text{N}$ -induced reactions on Ag and Au, whereas slope temperatures increase consistent with Fermi gas expectations, corrected for linear momentum transfer.

The results of EES calculations suggest the importance of emission time scale in the cooling of hot nuclei—which appears to be quite different for neutron-deficient and neutron excess isotopes. The EES model predicts that temperatures derived from IMF ratios reflect later, lower excitation-energy

stages of the cooling/disassembly process, whereas temperatures based on ${}^3\text{He}/{}^4\text{He}$ are more sensitive to the earlier stages. The time dependence of statistical emission, as well as feeding contributions as the emitted fragments cool, must also be folded into any interpretation of nuclear temperatures based on the double-isotope-ratio thermometer.

This analysis points to an evolutionary scenario for the deexcitation of hot nuclei [14,38,39]. The continuum of mechanisms that produces the final fragment observables begins with nonequilibrium emission processes that occur during the multiple-scattering stages between impact and equilibration. This is followed by the time-dependent cooling of the thermalized system, and in the case of the hottest systems, expansion and multifragmentation of the final residue. For the most highly-excited systems, the time scales for all of these stages: relaxation, thermal fluctuations and disassembly [39], occur on comparable time scales—preventing a clearcut separation in time. Finally, at every stage the primary fragment yields are perturbed by the secondary decay of the hot fragments.

ACKNOWLEDGMENTS

The authors wish to thank Betty Tsang for helpful discussions concerning isotope-ratio temperatures and for providing us with her tables of correction factors for sequential decay. We also acknowledge Wen-chen Hsi, Mike Carlson, Craig Helfgott, Doug Fields, Jay Wile, and Luc Beaulieu for various contributions to this work. We acknowledge the support of the U.S. Department of Energy (V.V. and K.K.), the National Science Foundation (W.A.F.), and the Indiana University Institute for Advanced Study (W.A.F.).

-
- [1] T.D. Thomas, Nucl. Phys. **53**, 558 (1964); **53**, 577 (1964).
 [2] D. Fabris *et al.*, Nucl. Phys. **A471**, 351c (1987).
 [3] K. Kwiatkowski, J. Bashkin, H. Karwowski, M. Fatyga, and V.E. Viola, Phys. Lett. B **171**, 41 (1986).
 [4] J.L. Wile *et al.*, Phys. Rev. C **45**, 2300 (1992).
 [5] W. Benenson, D.J. Morrissey, and W.A. Friedman, Annu. Rev. Nucl. Part. Sci. **44**, 27 (1994).
 [6] W. Bauer, Phys. Rev. C **51**, 803 (1995).
 [7] J. Pochodzalla *et al.*, Phys. Rev. C **35**, 1695 (1987).
 [8] D.H. Boal, C.K. Gelbke, and B.K. Jennings, Rev. Mod. Phys. **62**, 553 (1990).
 [9] J. Pochodzalla *et al.*, Phys. Rev. Lett. **75**, 1040 (1995).
 [10] J. Albergo, S. Costa, E. Costanzo, and A. Rubbino, Nuovo Cimento A **89**, 1 (1985).
 [11] R. Wada *et al.*, Phys. Rev. C **55**, 227 (1997).
 [12] Y.G. Ma *et al.*, Phys. Lett. B **390**, 41 (1997).
 [13] B. Hauger *et al.*, Phys. Rev. Lett. **77**, 235 (1996).
 [14] K. Kwiatkowski *et al.*, Phys. Lett. B **423**, 21 (1998); Advances in Nuclear Dynamics 4, edited by W. Bauer and H.G. Ritter (Plenum, New York, in press).
 [15] M.B. Tsang *et al.*, Phys. Rev. Lett. **78**, 3836 (1997); (private communication).
 [16] M.B. Tsang *et al.*, Phys. Rev. C **53**, R1057 (1996).
 [17] R.E.L. Green, R.G. Korteling, and K.P. Jackson, Phys. Rev. C **29**, 1806 (1984); R.E.L. Green, R.G. Korteling, J.M. D'Auria, K.P. Jackson, and R.L. Helmer, *ibid.* **35**, 1341 (1987).
 [18] J. Zhang, K. Kwiatkowski, D. Bonser, M. Fatyga, S.D. Coon, K. Stith, V.E. Viola, L.W. Woo, and S.J. Yennello, Phys. Rev. C **56**, 1918 (1997).
 [19] J. Brzychczyk, D.S. Bracken, K. Kwiatkowski, K.B. Morley, E. Renshaw, and V.E. Viola, Phys. Rev. C **47**, 1553 (1993).
 [20] J.E. Finn *et al.*, Phys. Rev. Lett. **49**, 1321 (1982).
 [21] M. Fatyga, K. Kwiatkowski, H. Karwowski, R. Byrd, and V.E. Viola, Phys. Lett. B **185**, 321 (1987); M. Fatyga, Ph.D. thesis, Indiana University, 1987.
 [22] J.R. Wu, C.C. Chang, and H.D. Holmgren, Phys. Rev. C **19**, 370 (1979); *ibid.* **19**, 659 (1979).
 [23] F. E. Bertrand and R.W. Peelle, Phys. Rev. C **8**, 1045 (1973).
 [24] L. Beaulieu and G.J. Wozniak, Lawrence Berkeley Laboratory (private communication).
 [25] W.A. Friedman, Phys. Rev. C **42**, 667 (1990).
 [26] A.M. Poskanzer, Lawrence Berkeley Laboratory (private communication).
 [27] E. Renshaw, S.J. Yennello, K. Kwiatkowski, R. Planeta, L.W. Woo, and V.E. Viola, Phys. Rev. C **44**, 2618 (1991).
 [28] R. Trockel *et al.*, Phys. Rev. C **39**, 729 (1989).
 [29] G. Kunde *et al.*, Phys. Lett. B **416**, 56 (1998).
 [30] F. Zhu *et al.*, Phys. Lett. B **322**, 43 (1994).
 [31] V. Serfling *et al.*, Phys. Rev. Lett. **80**, 3928 (1998).
 [32] D.J. Fields, W.G. Lynch, C.B. Chitwood, C.K. Gelbke, M.B.

- Tsang, H. Utsonomiya, and J. Aichelin, Phys. Rev. C **30**, 1912 (1984).
- [33] H. Xi *et al.*, Phys. Rev. C **67**, R462 (1998).
- [34] D.E. Fields, Ph.D. thesis, Indiana University, 1992.
- [35] D.S. Bracken, Ph.D. thesis, Indiana University, 1996.
- [36] V.E. Viola, Nucl. Phys. **A502**, 531 (1987).
- [37] L.G. Sobotka *et al.*, Phys. Rev. Lett. **51**, 2187 (1983).
- [38] R. Bougault *et al.*, in Proceedings of XXXV International Winter Meeting on Nuclear Physics, Bormio, Italy, 1997, edited by I. Iori, Suppl. no. 110, p. 251.
- [39] G. Wang *et al.*, Phys. Rev. C **57**, R2786 (1998).